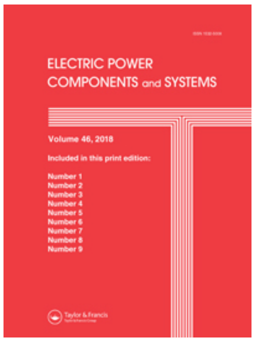

Electric Power Components and Systems

ISSN: 1532-5008 (Print) 1532-5016 (Online) Journal homepage: https://www.tandfonline.com/loi/uemp20

Design and Investigation of Low-cost PM Flux Switching Machine for Geared Medium-speed Wind Energy Applications

Udochukwu B. Akuru & Maarten J. Kamper

To cite this article: Udochukwu B. Akuru & Maarten J. Kamper (2018) Design and Investigation of Low-cost PM Flux Switching Machine for Geared Medium-speed Wind Energy Applications, Electric Power Components and Systems, 46:9, 1082-1090, DOI: 10.1080/15325008.2018.1485789

To link to this article: https://doi.org/10.1080/15325008.2018.1485789

Published online: 22 Dec 2018.

Electric Power Components and Systems, 46(9): 1082–1090, 2018

ISSN: 1532-5008 print / 1532-5016 online
DOI: 10.1080/15325008.2018.1485789

Taylor & Francis
Taylor & Francis Group

Check for updates

Design and Investigation of Low-cost PM Flux Switching Machine for Geared Medium-speed Wind Energy Applications

Udochukwu B. Akuru[1,2] and Maarten J. Kamper[1]
[1]Department of Electrical and Electronic Engineering, Stellenbosch University, Stellenbosch, South Africa
[2]Department of Electrical Engineering, University of Nigeria, Nsukka, Nigeria

CONTENTS

Abstract—There has been increasing innovation in research to harness nonconventional electrical machines *e.g.*, stator-mounted electrical machines like the flux switching machines (FSMs), in various applications such as wind power generation and electric traction. Hence, the need to further minimize the cost of electrical machines by avoiding designs using scarce rare-earth permanent magnets (PMs), especially if such machines were to be designed using PM materials. The approach in this article is to investigate the cost savings if a hitherto optimally designed 10 kW FSM which uses rare-earth PM is rather designed on less expensive ferrite PM for a medium-speed geared wind generator drive. Using 2D finite-element analyses and comparing the performance of two optimal benchmarks, it is shown that the ferrite design is heavier, leading to 61.2% reduction in the torque density compared to the rare-earth design. However, due to the high cost of rare-earth PMs, the active material cost of the ferrite design is found to be 35% cheaper. It is also found that due to deep saturation effects, the rare-earth design is more susceptible to demagnetization risks even within nominal load conditions, whereas the ferrite demagnetizes rapidly only beyond the nominal load.

1. INTRODUCTION

Lately, there is growing interest in the design of nonconventional electrical machines for wind energy applications [1]. Typical nonconventional machines are stator-active machines such as the flux switching machine (FSM), which have been a dominantly permanent magnet (PM) machine [2]. Already, the candidacy of the FSM for wind energy application is mounting as supported by some recent studies [3]–[6], however, only a handful of these studies have attempted using non-rare-earth PM excitation for geared medium-speed (MS) drivetrains [4] and [5]. Geared MS drivetrains are important because they reduce the gear box size to 1- or 2-stage from 3. Thus, unlike the traditional high-speed and low-speed drivetrains which have been popular for wind generator designs, MS designs (say

Keywords: demagnetization, ferrite permanent magnet (PM), finite element analyses (FEA), flux switching machine (FSM), geared medium-speed (MS), low-cost PM, rare-earth PM, wind energy, wind generator, saturation
Received 26 April 2017; accepted 20 May 2018
Address correspondence to Udochukwu B. Akuru, Department of Electrical Engineering, University of Nigeria, Nsukka 410001, Nigeria. E-mail: udochukwu.akuru@unn.edu.ng
Color versions of one or more of the figures in the article can be found online at www.tandfonline.com/uemp.

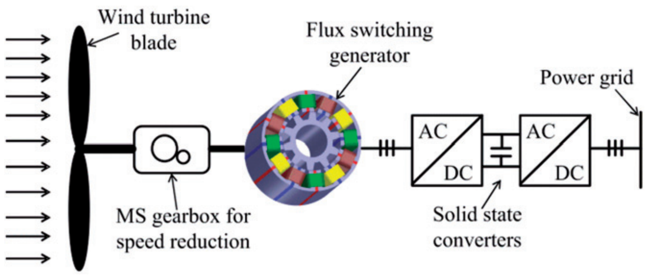

FIGURE 1. Proposed geared medium-speed wind energy system.

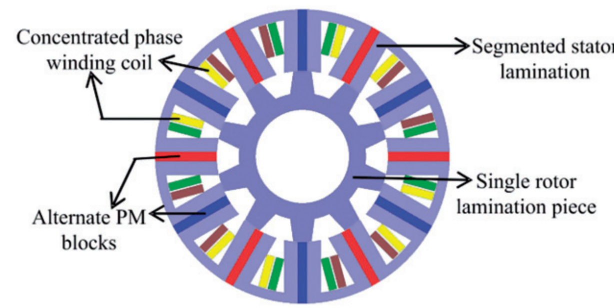

FIGURE 2. Cross-section of 12-stator slots/10-rotor pole PM-FSM.

100–600 r/min) provide moderation to the size and cost of both the gear and generator components [7].

Unlike rare-earths, ferrites are potentially cheaper (low-cost) PM options for FSMs (viz., PM-FSMs) and are bound to be more attractive to the industry. The high price of rare earths is mainly due to limited geographic sourcing, amidst a huge market potential for ferrites. It should equally be mentioned that the high demagnetization risks associated with ferrite PMs is potentially abated when used in the design of PM-FSMs due to a special magnetic circuitry [8].

To this end, this article will be used to investigate the optimal design of a 10 kW ferrite PM-FSM in contrast to its rare earth counterpart. Unlike a previous study which considered high-speed AC traction drives [9], the current study is designed for geared MS wind energy systems as shown in Figure 1. The main target is to minimize the active material mass, while maintaining acceptable machine performance. Thus, the article begins by providing background information on the design formulation of the FSM as a generator using a 2D static FEA-based optimization process. The subsequent sections are used to evaluate the performance of two optimized benchmark designs comprising a ferrite and a rare-earth PM-FSM generator. In the end, the results are corroborated based on counterpart 2D and 3D transient FEA solutions.

2. DESIGN PROCESS

2.1. Basic Structure and Design Formulation of PM-FSMs

FSMs are identified as machines of robust structure and high power density, with essentially bipolar phase flux linkages and sinusoidal back-EMF waveforms. The earliest version of the PM-FSM featured a simple radial-flux design [10]. Nowadays, especially for low-speed wind generator drives, axial-flux [11], as well as transverse-flux [12] PM-FSMs exists, although these are defined by very complicated design features. Among existing radial-flux PM-FSM topologies today, the 3-phase 12/10 (12-stator-slots/10-rotor-pole) topology as shown in Figure 2 has been popularized. The 12/10 PM-FSM configuration is well adapted to the MS drive regimes. Thus, it is selected for the proposed design process. The design process is illustrated in the flowchart given in Figure 3. Both the ferrite and rare-earth PM-FSMs are subjected to almost the same design specifications as advanced in Table 1. Note that the different stator outer diameters realized for the ferrite and rare-earth PM-FSM designs as indicated in Table 1 is simply based on the sizing equation highlighted in [13], with approximations for fixed frame sizes.

2.2. Analytical Equations

The 3-phase magnetic axes of the 12/10 PM-FSM can be easily analyzed by transforming them into the traditional direct axis (d-axis) and quadrature axis (q-axis) parameters notably referred to as dq-axes components. The simplified dq equivalent circuit of PM-FSMs is as shown in Figure 4. Thus, the voltage equations, while assuming generator operation, may be approximated as

$$V_d = -R_s I_d + X_q I_q, \tag{1}$$

$$V_q = -R_s I_q - X_d I_d + E_q, \tag{2}$$

where E_q is the generated internal voltage. X_d and X_q are, respectively, the dq-axes reactances which are equal to the sum of the magnetizing, phase-winding leakage and phase end-winding reactances. The end-winding reactance effects have been computed as formulated in [13]. The expression for the electromagnetic torque and torque ripple is given as

$$T_e = \frac{3}{2} N_r \left(I_q \lambda_M + \left(\frac{X_d - X_q}{\omega_e} \right) I_d I_q \right), \tag{3}$$

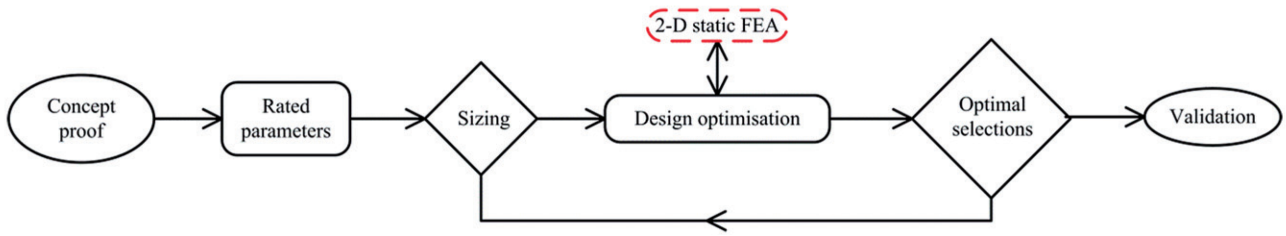

FIGURE 3. Work flow for PM-FSM design process.

	Rare-earth	Ferrite
Stator outer diameter (D_{out})	250 mm	350 mm
PM remanence	1.2 T	0.4 T
Number of turns per slot	100	
Fill factor ratio per half slot	0.45	
Shaft speed (ω_s)	360 r/min	
Output power	$P_{out} \geq 10\,\text{kW}$	
Efficiency	$\eta \geq 90\%$	
Power factor	$\cos\phi \geq 0.8$	
Ripple torque	$k_\delta \leq 10\%$	

TABLE 1. Design targets and parameter specifications.

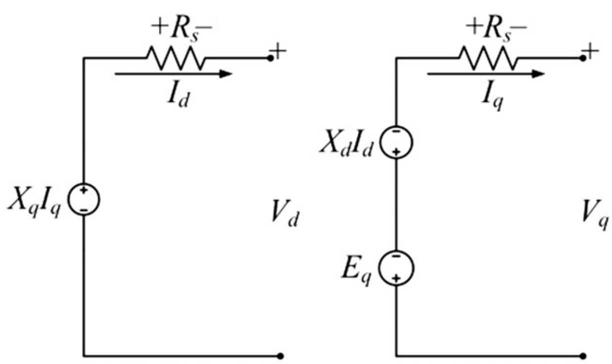

FIGURE 4. PM-FSM dq equivalent circuits.

$$k_\delta = \frac{T_{e(\max)} - T_{e(\min)}}{T_e}, \tag{4}$$

where N_r is the rotor teeth number, λ_M is the flux linkage solely due to the field type, ω_e is the electrical speed in rad/s, $T_{e(\max)}$ and $T_{e(\min)}$ are the maximum and minimum peaks of T_e when the machine is operating on load.

Under steady-state generator operation, the PM-FSM phasor diagram as shown in Figure 5 shows the power factor angle as a function of load (Δ) and current (α) angles given as

$$\phi = \alpha + \Delta. \tag{5}$$

The PM-FSM generator output power as derived from the dq axes variables, as well as the generator efficiency is given as

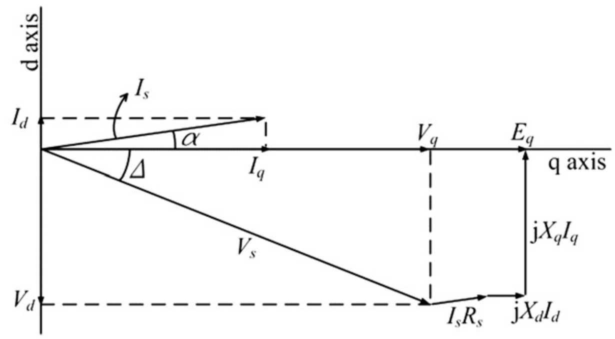

FIGURE 5. PM-FSM vector diagram.

$$P_{out} = \frac{3}{2}(V_d I_d + V_q I_q), \tag{6}$$

$$\eta = \frac{P_{out}}{P_{out} + P_{Cu} + P_{core}}. \tag{7}$$

The copper losses (P_{Cu}) and the core losses (P_{core}), which is defined by the summation of the hysteresis and eddy current losses, are expressed as

$$P_{Cu} = \frac{3}{2}\left(I_d^2 + I_q^2\right)R_s, \tag{8}$$

$$P_{core} = C_m\left(f_e^\beta\left(\dot{B}_{st}^\sigma M_{st} + \dot{B}_{sy}^\sigma M_{sy}\right) + f_{re}^\beta\left(\dot{B}_{rt}^\sigma M_{rt} + \dot{B}_{ry}^\sigma M_{ry}\right)\right), \tag{9}$$

where C_m, σ, and β are Steinmetz coefficients determined by experiments from frequency (f_e), $\dot{B}_{st}$ is the peak flux density in the stator tooth, M_{st} is the total mass of the stator teeth, $\dot{B}_{sy}$ is the peak flux density in the stator yoke, M_{sy} is the total mass of the stator yoke, $\dot{B}_{rt}$ is the peak flux density in the rotor tooth, M_{rt} is the total mass of the rotor teeth, $\dot{B}_{ry}$ is the peak flux density in the rotor yoke, and M_{ry} is the total mass of the rotor yoke. Note that f_{re} is a factor of f_e introduced because the rotor experiences reduced core losses (usually 30–40%) compared to that of the stator [15]. The phase resistance, R_s, is calculated as

$$R_s = \frac{8N_{ph}^2 \rho_{Cu(l_{st}+l_e)}}{A_{ph}}, \tag{10}$$

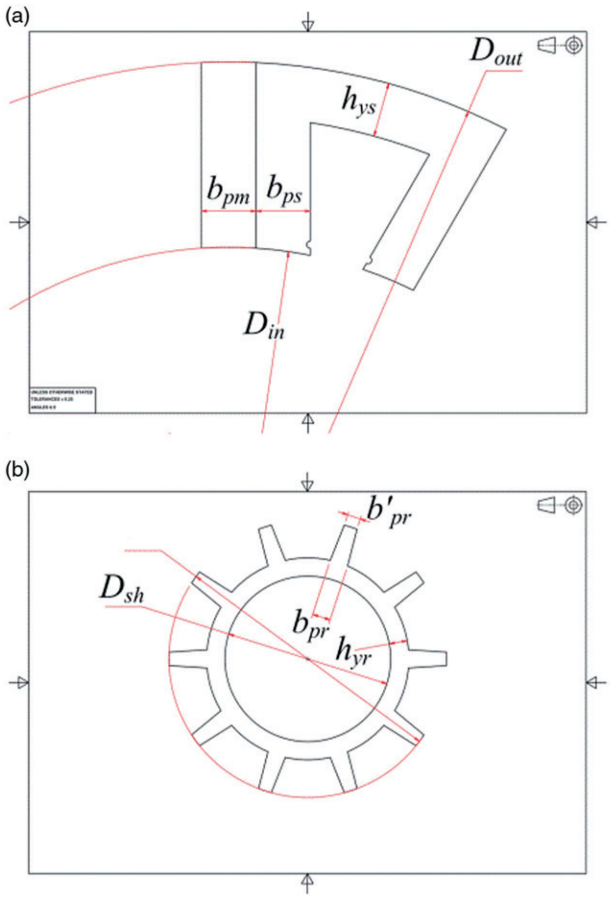

FIGURE 6. Cross-sectional views of PM-FSM dimensional variables: (a) stator and (b) rotor.

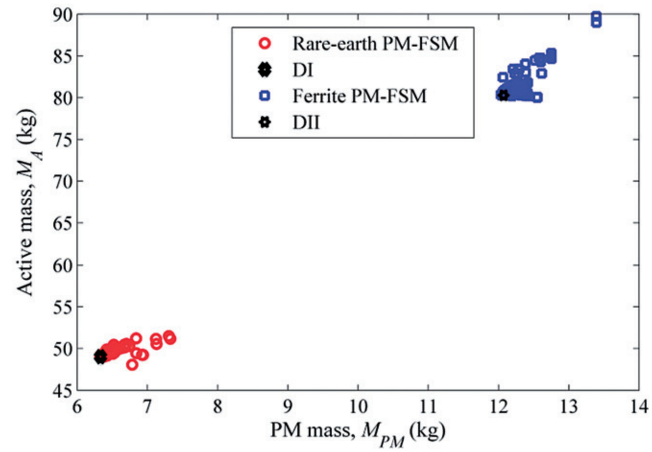

FIGURE 7. Display of the evolved optimal colonies.

where N_{ph} is the turns number per coil for the phase windings, ρ_{Cu} is the resistivity of copper at room temperature, l_{st} is stack length of the iron laminations, l_e is the end-winding length of the copper conductors evaluated using the method prescribed in [13], and A_{ph} is the area per coil for the phase. The constant number coefficient in (10) is indicative of the slot arrays for series connection of the phase windings. Note that the conductor eddy current losses due to skin effects have been ignored because they are considered negligible within the nominal load operation of conventional PM-FSMs [14].

2.3. Design Optimization

The optimization process involved a non-gradient multi-objective algorithm evaluated in FEA. It takes into account the simultaneous evaluation of two objective functions, namely; the PM mass (M_{PM}) and the total active mass (M_A). The design constraints as indicated in Table 1 are meant to limit the proposed generator performance within acceptable operating points. The design variables to be optimized is described by the transposed vector X given as

$$X = \begin{bmatrix} \alpha & J & l_{st} & D_{in} & D_{sh} & b_{pm} & b_{pr} & b_{sls} & h_{ys} & h_{yr} & t_0 \end{bmatrix}^T, \tag{11}$$

X	Parameters	Rare-earth (DI)	Ferrite (DII)
α	Current angle (°)	89.984	89.997
J	Phase current density (A/mm^2)	4.982	3.607
l_{st}	Stack length (mm)	178.948	165.529
D_{in}	Stator inner diameter (mm)	146.287	220.626
D_{sh}	Shaft diameter (mm)	80.029	119.879
b_{PM}	PM length (mm)	7.582	18.793
b_{pr}	Rotor pole width (mm)	20.438	24.004
b_{sls}	Slot opening width (mm)	7.282	13.801
h_{ys}	Stator yoke height (mm)	7.711	18.420
h_{yr}	Rotor yoke height (mm)	13.784	18.750
t_0	Rotor teeth taper factor	0.738	0.850

TABLE 2. Optimal design parameters.

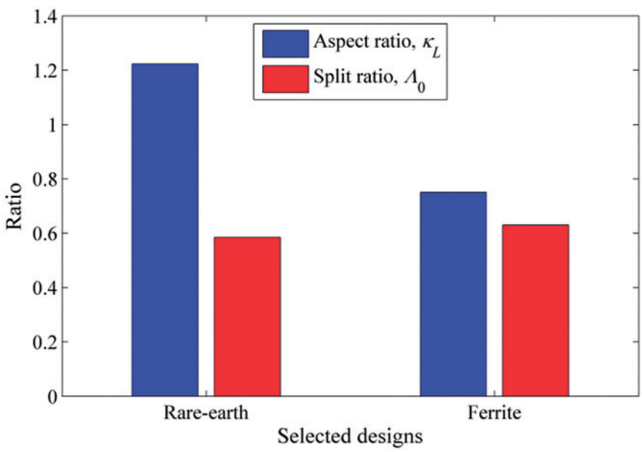

FIGURE 8. Comparison of aspect and split ratios.

where J is the phase current density, D_{in} is the stator inside diameter, D_{sh} is the shaft diameter, b_{pm} is the PM width, b_{pr} is the rotor pole width, b_{sls} is the slot opening width, h_{ys} is the stator yoke height, h_{yr} is the rotor yoke height, and t_0 is a tapering factor for the rotor teeth defined as the ratio $b_{pr} : b'_{pr}$. The remaining variables have been earlier defined. The total number of decision variables as denoted in X is 11, and illustrated as shown in Figure 6, with the exception of J and l_{st} which are not displayed.

A total of 2,000 function evaluations are computed with a population size of 20 at 100 generations. Key parameter settings such as the crossover probability, crossover distribution index and mutation distribution index were tuned to 0.95, 10 and 15, respectively. The mutation probability is taken as the inverse of the number of decision variables for each problem type. Based on a Core i7 CPU 16 GB RAM workstation, it required approximately 30 h to exhaust one optimization run.

2.4. Results and Discussions

The design optimization results are displayed by the scatter plots in Figure 7, which clearly shows a wide margin separating the colonies of the optimal set of the evaluated PM-FSM variants. At a closer look, it is observed that the ferrite PM-FSMs requires at least 1.5 times of the active mass and 2 times of the PM mass that of the rare-earth PM-FSMs. From the broadcasted results in Figure 7, two sample designs, one from each PM-FSM variants, are benchmarked for further evaluation. As shown, the selected designs are highlighted in the optimal design collections as DI (for the rare-earth PM-FSM) and DII (for the ferrite PM-FSM).

Table 2 is used to show the optimum design parameters obtained for the two selected designs. It is observed that for the same design requirements, the optimal PM mass per active mass results in a narrower PM length and longer stack length for the rare-earth design, compared to the ferrite PM-FSM. The ratio of PM length to stack length is 4.2% in the former, compared to 11.3% in the latter. This observation is due to the fact that PM-FSMs have flux focusing capabilities which enables a thinner PM length in this instance, encouraged by the superior quality of rare-earth PM compared to ferrite PM.

The aspect ratio ($K_L = \frac{l_{st}}{D_{in}}$) and split ratio ($\Lambda_0 = \frac{D_{in}}{D_{out}}$) of the optimal design candidates are both contested as shown in Figure 8. The illustration shows that the aspect ratio, more than the split ratio, is critical for the optimal performance of the rare-earth design. As for the lower quality ferrite PM, the split ratio is widened in correspondence to strengthening of the airgap magnetic field.

Meanwhile, the discrepancy in current densities in Table 2 can be related to the copper losses viz., the

	Units	Rare-earth	Ferrite	Slip (%)
Average torque, T_e	Nm	259.23	258.48	0.29
Torque ripple, k_δ	%	7.84	9.42	−16.77
Cogging torque, $k_{\delta 0}$	%	6.42	12.65	−49.24
Stator iron mass	kg	23.84	36.42	−34.54
Rotor iron mass	kg	10.02	18.91	−47.01
Copper mass	kg	6.95	9.19	−24.37
PM mass	kg	6.33	12.07	−47.55
Active mass	kg	47.15	76.59	−38.43
Copper loss, P_{Cu}	W	447.92	341.63	31.11
Core loss, P_{core}	W	188.17	163.15	15.33
Output power	kW	9.99	9.97	0.20
Machine efficiency, η	%	94.01	95.18	−1.22
Power factor	–	0.79	0.79	0
Torque/active mass, τ_{pa}	Nm/kg	5.50	3.37	63.20

TABLE 3. Performance indices.

Item	Cost (USD/kg)
NdFeB PM	60
Ferrite PM	10
Copper	11.2
Iron lamination	2.2

TABLE 4. Cost quote of materials [9].

	Rare-earth	Ferrite
Coercive force, H_c (kA/m) (at 20 °C)	900	258
PM remanence, B_r (T)	1.2	0.4
Relative permeability, μ_r	1.06	1.06
Mass density (kg/m^3)	7,500	5,000

TABLE 5. Characteristics of selected PMs.

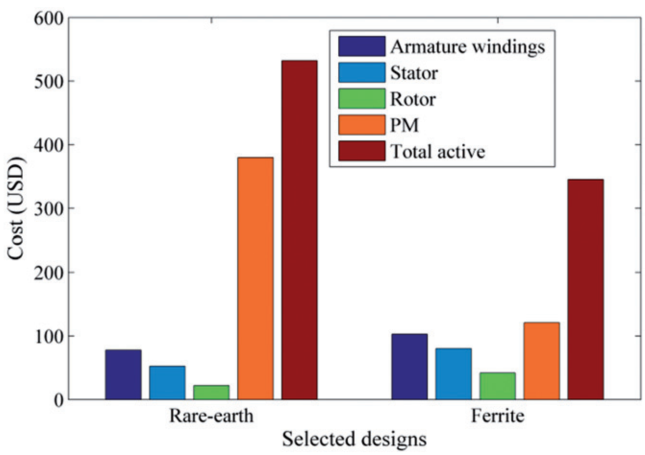

FIGURE 9. Comparison of different material costs.

efficiency in Table 3. Since the theoretical slot filling factor and conductor number per coil of both designs is kept constant as indicated in Table 1, one can infer that a higher current density value corresponds to higher copper loss, which in this case slightly reduces the efficiency of the rare-earth PM-FSM.

Table 3 gives a summary of both PM-FSM designs attaining the prescribed design targets. However, the torque density for the rare-earth design is seen to be 63.2% more than the ferrite, thanks to a smaller generator head mass. But from an economic standpoint, the total active material cost of the ferrite design is 65% compared to the rare-earth design, based on price quotations shown in Table 4. Consequently, the higher total cost of the rare-earth design is driven primarily by more expensive rare-earth PMs as illustrated by the cost breakdown of components shown in Figure 9.

3. DEMAGNETIZATION RISKS

A common characteristic of PMs is their demagnetization susceptibility at high temperatures or as a result of excessive currents in the associated windings [15]. Ordinarily, a drop in magnetic coercivity (negative H_c) in a typical PM demagnetization curve is indicative of proportional temperature rise, although this generalization is not applicable to ferrites and Alnico because of their positive temperature coefficients, which mean that they perform better as they get hotter [16]. Besides, ferrites, unlike rare-earths, are not prone to eddy current losses, also meaning that their electrical resistance is very high [17]. This goes to show that the quality of the PM material used is also a factor of its demagnetization characteristics.

In this section, the demagnetization resistance of the ferrite and rare-earth PM-FSM optimal benchmarks is

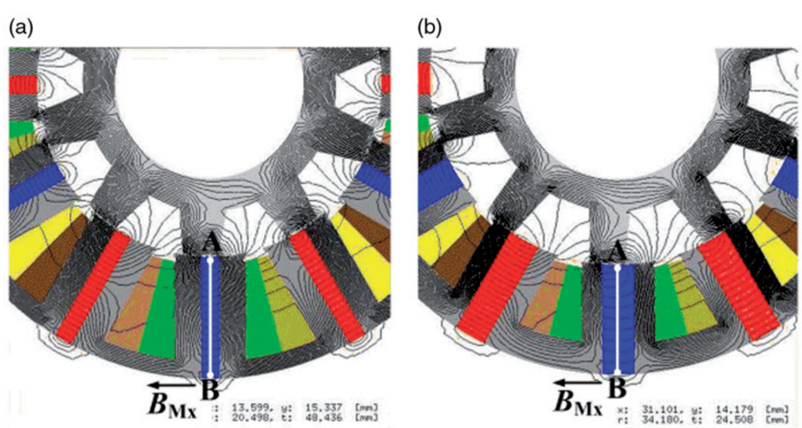

FIGURE 10. 2D static FEA distribution of PM-FSM reference normal to flux lines in the x-direction of the PMs: (a) rare-earth and (b) ferrite.

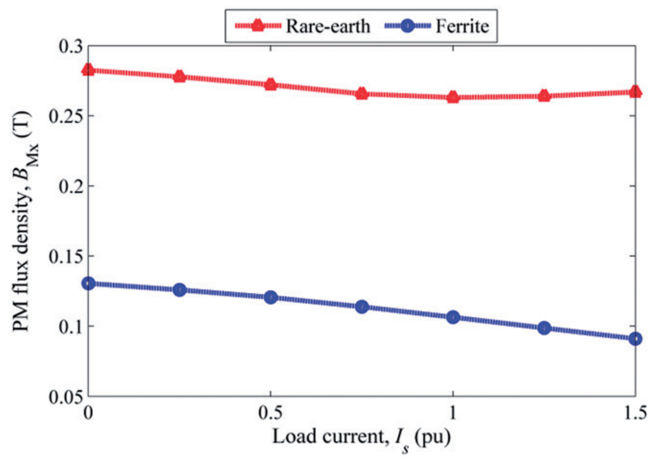

FIGURE 11. Average PM flux density under different load conditions.

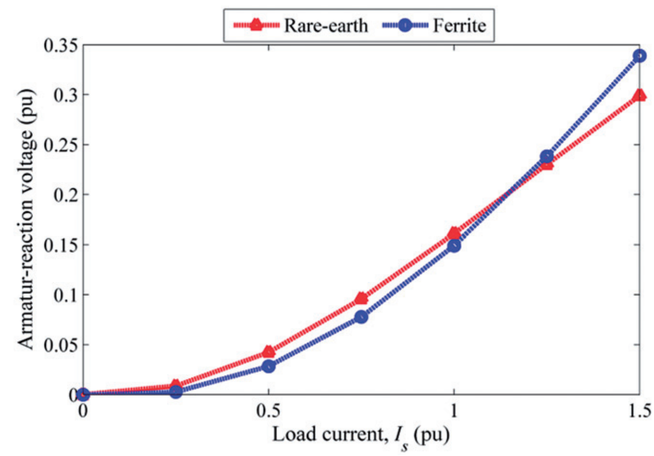

FIGURE 12. Load profile of normalized armature-reaction voltages at 360 r/min.

undertaken by using static FEA solution to appraise the impact of the load currents on the PM remanence (B_r). The characteristics of the ferrite and rare-earth PMs used in the study is provided in Table 5. The demagnetization characteristics of both machines are investigated using the average flux density component normal to the field lines along the x-direction, illustrated by points "A" and "B" in Figure 10. As indicated in [9], the prescribed safety limit of flux density normal to PM flux lines for the rare-earth PM is given as $B_n > 0.4\,\text{T}$ at maximum temperature of 120 °C, while that of ferrite PM is $B_n > 0.1\,\text{T}$ at minimum temperature of 20 °C. The PM position where the magnitude is lowest for a given static FEA solution is thus considered. But, it should be mentioned that the demagnetization levels considered in this study are mainly evaluated based on the magnetic saturation effects of the load currents on the PMs.

In Figure 11, based on the evaluated load profile, the rare-earth design was unable to satisfy the safety limit (*i.e.*, $B_{Mx} < 0.4\,\text{T}$), unlike the ferrite design (*i.e.*, $B_{Mx} > 0.1\,\text{T}$). The main reason for this disparity is due to the high cross-magnetization effects of the current-induced magnetic fields in the former, resulting in higher armature-reaction effects between no-load and nominal load regimes as portrayed in Figure 12. On the other hand, beyond the nominal load as shown in Figure 12, the safety limit for the ferrite design is not respected. Apparently, this results in rapid saturation when the ferrite design becomes overloaded. To corroborate the results in Figures 11 and 12, the flux density contour plots are shown in Figure 13, under rated conditions. A higher degree of demagnetization at the PM edges of the rare-earth design compared to that of the ferrite is clearly depicted, especially towards the airgap. Overall, it can be said that the ferrite design can be operated with minimum

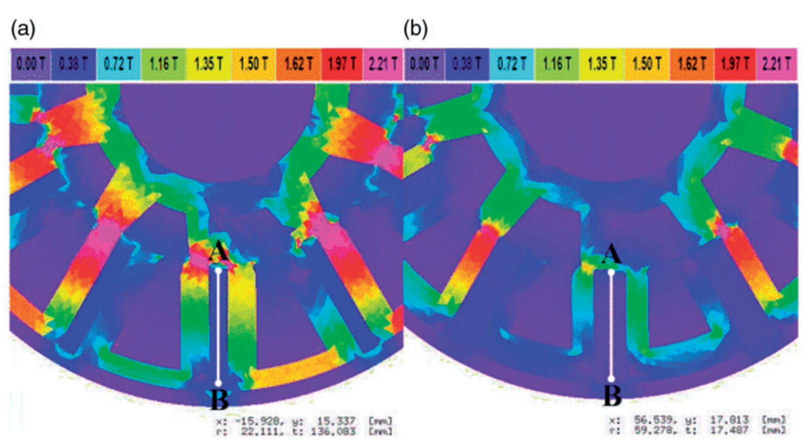

FIGURE 13. Contour plots of PM flux densities at rated conditions: (a) rare-earth design and (b) ferrite design.

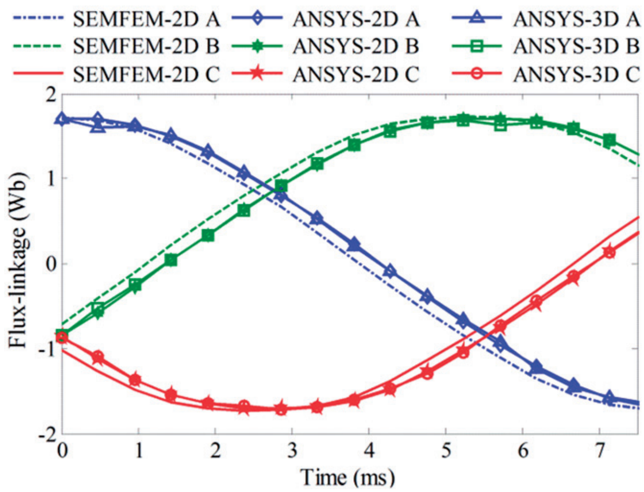

FIGURE 14. Comparison of flux linkages in rare-earth PM-FSM at no load.

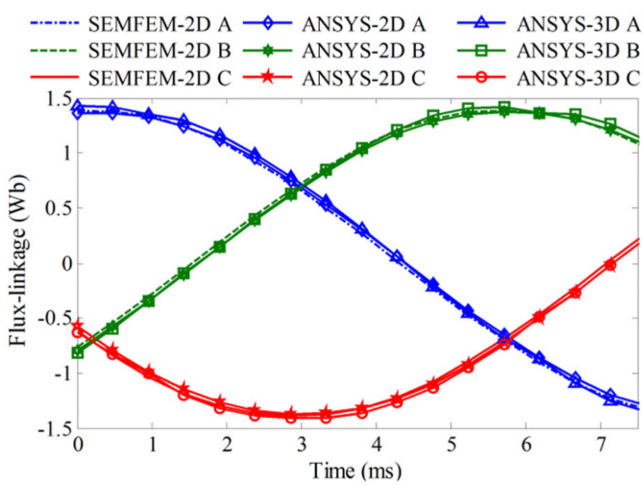

FIGURE 15. Comparison of flux linkages in ferrite PM-FSM at no load.

demagnetization risks at load current values not exceeding nominal condition. Suffice to say that the emphasis on the nominal condition is based on the fact that such operating regime is the most dominant range between the cut-in and cutout points in the wind speed bands of the proposed variable-speed wind turbines [18]. Hence, the deep saturation of the rare-earth design, before the nominal load regime, raises demagnetization concerns.

4. VALIDATION

So far, the results provided have been based on non-linear 2D FEA magnetostatic solutions using SEMFEM [19]. In this section, counterpart transient solutions in 2D and 3D FEA using ANSYS Maxwell© environment is undertaken to verify the obtained preliminary results. In Figures 14 and 15, the flux linkages at no-load conditions, which have been graphically compared for the different FEA simulations, exhibit close correlation. The good match is an indication that the end-winding effects in static 2D FEA are correctly approximated.

5. CONCLUSION

The design and investigation of low-cost permanent magnet flux switching machines (PM-FSMs) for geared medium-speed wind energy applications has been studied in this article. Two PM-FSM variants (one designed with ferrite PM and the other designed using rare-earth PM) were optimized, analyzed, and verified in different 2D and 3D finite element evaluations, at 10 kW power levels. Based on similar performance requirements, the toque density of the ferrite PM-FSM is 61.2% that of the rare-earth PM-FSM, but with an estimated material cost savings of 35%. It is also found that deep saturation occurs in the rare-earth design, which lowers its demagnetization withstand ability, even while operating below the nominal load. On the contrary, the ferrite design only records high demagnetization risks at load current values above rated, although the demagnetization rate rapidly increases afterwards. The fact that the demagnetization risks for the ferrite is minimal below rated condition is a key finding, especially for such low quality grade PMs. Moreover, the regime below the nominal load is the dominant operating region for the proposed wind energy application; thus making the ferrite PM-FSM a suitable candidate as both a low-cost and robust design.

REFERENCES

[1] U. B. Akuru, and M. J. Kamper, "Contemporary wind generators," *J. Energy South. Afr.*, vol. 26, no. 3, pp. 116–124, Aug. 2015.
[2] M. Cheng, W. Hua, J. Zhang, and W. Zhao, "Overview of stator-permanent magnet brushless machines," *IEEE Trans. Ind. Electron.*, vol. 58, no. 11, pp. 5087–5101, 2011.
[3] P. Andrada and F. Martinez, "Flux switching alternators for small wind generation," ICREPQ'16, Madrid, Spain, 2016.
[4] Y. Wang, J. Sun, Z. Zou, Z. Wang, and K. T. Chau, "Design and analysis of a HTS flux-switching machine for wind energy conversion," *IEEE Trans. Appl. Supercond.*, vol. 23, no. 3, pp. 5000904–5000904, Jun. 2013.
[5] U. B. Akuru and M. J. Kamper, "Performance comparison of optimum wound-field and ferrite PM flux switching machines for wind energy applications," XXII International

Conference on Electrical Machines (ICEM), Lausanne, 2016, pp. 2478–2485.

[6] C. H. T. Lee, K. T. Chau, and C. Liu, "Design and analysis of a dual-mode flux-switching doubly salient DC-field magnetless machine for wind power harvesting," *IET Renew. Power Gen*., vol. 9, no. 8, pp. 908–915, 2015.

[7] S. Schmidt and A. Vath, "Comparison of existing medium-speed drive train concepts with a differential gearbox approach," European Wind Energy Association, EWEA, Copenhagen, Apr. 2012, pp. 179–186.

[8] J. D. McFarland, T. M. Jahns, and A. M. El-Refaie, "Demagnetization performance characteristics of flux switching permanent magnet machines," International Conference on Electrical Machines (ICEM), Berlin, Germany, 2014, pp. 2001–2007.

[9] A. Fasolo, L. Alberti, and N. Bianchi, "Performance comparison between switching-flux and IPM machines with rare-earth and ferrite PMs," *IEEE Trans. Ind. Appl*., vol. 50, no. 6, pp. 3708–3716, Nov.–Dec., 2014.

[10] S. E. Rauch and L. J. Johnson, "Design principles of flux-switching alternators," *AIEE Trans*., vol. 74III, pp. 1261–1268, 1955.

[11] M. Lin, L. Hao, X. Li, X. Zhao, and Z. Q. Zhu, "A novel axial field flux-switching permanent magnet wind power generator," *IEEE Trans. Magn*., vol. 47, no. 10, pp. 4457–4460, Oct. 2011.

[12] J. Yan, H. Lin, Y. Huang, H. Liu, and Z. Q. Zhu, "Magnetic field analysis of a novel flux switching transverse flux permanent magnet wind generator with 3-D FEM," International Conference on Power Electronics and Drive Systems, 2009. PEDS 2009, Nov. 2–5, 2009, pp. 332–335.

[13] U. B. Akuru and M. J. Kamper, "Formulation and multi-objective design optimisation of wound-field flux switching machines for wind energy drives," *IEEE Trans. Ind. Electron*., vol. 65, no. 2, pp. 1828–1836, 2018.

[14] J. T. Chen and Z. Q. Zhu, "Losses and efficiency in alternate switched-flux permanent magnet machines," *COMPEL*, vol. 31, no. 1, pp. 54–70, 2011.

[15] S. D. Umans, *Fitzgerald & Kingsley's Electric Machinery*, 7th ed. New York: McGraw-Hill International Edition, 2014.

[16] S. Sjökvist, "Demagnetisation studies on permanent magnets – comparing FEM simulations with experiments," Licentiate thesis, Uppsala Universitet, Jun. 2014.

[17] E. Nipp, "Permanent magnet motor drives with switched stator windings," Doctoral thesis, Royal Institute of Techonology, Stockholm, May 1999.

[18] M. G. Simões, F. Alberto Farret, and F. Blaabjerg, "Small wind energy systems," *Electric Power Compon. Syst*., vol. 43, no. 12, pp. 1388–1405, 2015.

[19] S. Gerber, "A finite element based optimisation tool for electrical machines," MSc thesis, Department of Electrical and Electronic Engineering, Stellenbosch University, Stellenbosch, South Africa, Mar. 2011.

BIOGRAPHIES

Udochukwu B. Akuru was born in Lagos, Nigeria, on June 6, 1983. He obtained the PhD degree in Electrical Engineering from Stellenbosch University, South Africa in December 2017, and both the MEng and BEng degrees from University of Nigeria, Nsukka, in June 2013 and August 2008, respectively. He is lecturing at University of Nigeria, Nsukka, but on secondment at Stellenbosch University, South Africa, as a postdoctoral research fellow. He is a registered member of the Council for the regulation of Engineering in Nigeria (COREN), Member of IEEE and volunteer to its associated societies, committees and groups. Dr. Akuru has a number of peer-reviewed journal and conference papers, and also acts as a reviewer to international conferences and journals. His main research interests are in electrical drives and renewable energy technologies with competency in finite element analyses and optimization of electrical machines.

Maarten J. Kamper received the MSc (Eng) degree in 1987 and PhD degree in 1996, both from the University of Stellenbosch, Stellenbosch, South Africa. He has been with the academic staff of the Department of Electrical and Electronic Engineering, University of Stellenbosch, since 1989, where he is currently a professor of electrical machines and drives. Prof. Kamper is a South African National Research Foundation Supported Scientist and a Registered Professional Engineer in South Africa. His research interests include computer-aided design and control of reluctance, permanent magnet, and inductance machine drives.